

Chirol, Clementine, Carr, Simon ORCID: <https://orcid.org/0000-0003-4487-3551> , Spencer, Kate L. and Moeller, Iris (2021) Pore, live root and necromass quantification in complex heterogeneous wetland soils using X-ray computed tomography. *Geoderma*, 387 . p. 114898.

Downloaded from: <http://insight.cumbria.ac.uk/id/eprint/5896/>

Usage of any items from the University of Cumbria's institutional repository 'Insight' must conform to the following fair usage guidelines.

Any item and its associated metadata held in the University of Cumbria's institutional repository Insight (unless stated otherwise on the metadata record) may be copied, displayed or performed, and stored in line with the JISC fair dealing guidelines (available [here](#)) for educational and not-for-profit activities

provided that

- the authors, title and full bibliographic details of the item are cited clearly when any part of the work is referred to verbally or in the written form
 - a hyperlink/URL to the original Insight record of that item is included in any citations of the work
- the content is not changed in any way
- all files required for usage of the item are kept together with the main item file.

You may not

- sell any part of an item
- refer to any part of an item without citation
- amend any item or contextualise it in a way that will impugn the creator's reputation
- remove or alter the copyright statement on an item.

The full policy can be found [here](#).

Alternatively contact the University of Cumbria Repository Editor by emailing insight@cumbria.ac.uk.

1 Pore, live root and necromass quantification in
2 complex heterogeneous wetland soils using X-ray
3 Computed Tomography

4 *Clementine Chirol*, Simon Carr, Kate Spencer, Iris Moeller*

5 *School of Geography, Queen Mary University London, Mile End Road, E1 4NS, London, UK*

6 KEYWORDS: X-ray computed tomography, sediment, microstructure, porosity, live roots,
7 necromass, soil carbon dynamics

8

9 ABSTRACT: Subsurface structures and especially the interactions between pores, roots and other
10 organic matter elements have a strong impact on ecosystem functioning. Yet despite recent
11 progress in the application of X-ray Computed Microtomography (μ CT) to soil structure in
12 agricultural science, applications to the more complex and heterogeneous substrates found in
13 natural soils, specifically wetland soils, remain sparse. We apply X-ray μ CT to a complex
14 heterogeneous soil and develop a robust segmentation method to quantify the pores, live roots and
15 necromass. This approach significantly improves the detection of the organic matter elements, and
16 gives us unprecedented detail and resolution in the segmentation of pores, live roots and necromass
17 at a high spatial resolution ($62.5 \mu\text{m}$ in this study). We identify several situations where pores and

18 organic matter interact in the soil, including the disconnected air spaces (aerenchyma) that run
19 within the *Spartina* stem and roots, tubular-shaped pores left behind by decaying roots, and lateral
20 roots deploying within structural fragilities in the sediment. The capacity of X-ray μ CT to
21 distinguish the connected live root system from the necromass opens possibilities for applications
22 to determine key wetland soil functions such as soil cohesivity, soil nutrient exchanges and soil
23 carbon dynamics.

24 **1. Introduction**

25
26 Soils and sediments, formed respectively from the in-situ weathering of a bedrock in association
27 with biogeochemical processes (Lin, 2010) and from the layered deposition of imported particles
28 (Dyer, 1995), both play a critical role for the ecosystems they support. They are a place of
29 exchange of water, gases and other resources, while providing structural support and shelter for
30 dwelling organisms (Rabot et al., 2018). The structure of these subsurface environments, defined
31 as the three-dimensional spatial arrangement of solids regardless of chemical heterogeneity
32 (Rabot et al., 2018; Xiong et al., 2019), results from the unique pedological (soil) and
33 hydrodynamic (sediment) history of each habitat and is dynamic over multiple spatial and
34 temporal scales. Because of this heterogeneity, structural properties (e.g. the measurable
35 components of the soil structure, such as total porosity) are difficult to describe, yet doing so can
36 greatly improve our understanding of ecosystem functions. Structure conditions
37 geomorphological, pedological and ecological functioning (Corenblit et al., 2011; Lin, 2010;
38 Rabot et al., 2018) and soil/sediment mechanics (Fonseca et al., 2013; Keller et al., 2013;
39 Menzies et al., 2016; Phillips et al., 2018; Spagnolo et al., 2016). Structure notably controls the
40 soils' interactions with the surface by providing pathways for gas, water and solute fluxes (Ball,

41 2013; Dale et al., 2019; Gharedaghloo et al., 2018; Pedersen et al., 2015; Spencer et al., 2017;
42 Swanson et al., 2017). Live roots also provide pathways of gas and nutrient exchanges, and play
43 an important role in soil carbon dynamics (Bardgett et al., 2014; Blagodatsky & Smith, 2012;
44 Smith et al., 2003). Due to these combined functions, structure exerts a critical control over
45 soil/sediment fertility and agricultural potential (Naveed et al., 2016; Pöhlitz et al., 2018; Rogers
46 et al., 2016).

47 Because of the complexity of soil and sediment structure, its influence on ecosystem processes
48 cannot be accurately predicted by one-dimensional parameters measured from traditional
49 methods in the field or in the lab (Bradley & Morris, 1990). 3D X-ray Computed Tomography
50 (CT) utilizes the penetrating capacity and attenuation of X-ray energy to image the 3D internal
51 structure and relative densities of materials ('phases') in a non-destructive manner (Cnudde &
52 Boone, 2013). The technique, developed for medical applications in the 1970s, soon led to the
53 higher resolution method X-ray Computed Microtomography (μ CT) in the 1980s and to the
54 study of microstructures in the geological and soil sciences (Ketcham and Carlson, 2001;
55 Ketcham, 2005; Carlson, 2006; Taina et al., 2008; Cnudde and Boone, 2013). In soil sciences,
56 the application of μ CT has largely focused on agricultural soils (Helliwell et al., 2013; Keller et
57 al., 2013; Menon et al., 2020; Mooney, 2002; Rogers & Benfey, 2015; Wildenschild &
58 Sheppard, 2013). By contrast, lacustrine, estuarine, glacial, fluvial and marine sediments and
59 associated soils typically represent multiple sediment sources, with mixing and superposition of
60 different minerogenic and biogenic components with variable water content (Bendle et al., 2015;
61 Dale et al., 2019; Griggs et al., 2015; Spagnolo et al., 2016; Spencer et al., 2017; Tarplee et al.,
62 2011; Voepel et al., 2019). This leads to significant textural and structural heterogeneities in
63 samples, which challenges the data acquisition and analysis approaches developed for the

64 examination of more homogenous agricultural soils. Here, we have focused on heterogeneous,
65 tidally flooded saltmarshes which retain both sedimentary (e.g. laminations) and pedological
66 (e.g., vegetation) features and are commonly referred to as soils. Therefore, for simplicity, we
67 use the term soils to include also unconsolidated and/or vegetated sediments deposited in aquatic
68 environments with minerogenic and biogenic components, as they present characteristics of both
69 sediments and soils.

70 The acquisition and interpretation of μ CT imagery of heterogeneous soils poses technical
71 challenges. Firstly, such soils are often unconsolidated and saturated, and therefore easily
72 disturbed, making recovery of ‘undisturbed’ samples very difficult, particularly at depth (Carr et
73 al., 2020). Secondly, samples with significant physical heterogeneity are challenging to
74 ‘segment’ into relevant phases based on X-ray attenuation coefficient alone. The segmentation
75 process is further complicated where there is a significant component of fine-grained sediments
76 below the spatial resolution of the scanning system (e.g. $<60\mu\text{m}$ in this study), whereby an
77 individual voxel in the reconstructed 3D volume represents the mean attenuation coefficient of
78 all elements present within. The intermediate grayscale value resulting from that mix of phases is
79 called the partial volume effect (Ketcham & Carlson, 2001); the more heterogenous and fine-
80 grained the material, the harder it becomes to isolate key phases based on their grayscale values
81 alone using global thresholding (Cnudde & Boone, 2013; Helliwell et al., 2013). Thirdly, most
82 soils, particularly those formed in aquatic environments such as wetland soils, contain variable
83 amounts of pore-water, meaning that the pore phase itself will be heterogeneous, with pores
84 being air-filled, water-filled, and often a combination of these states. Vegetated environments
85 such as coastal wetlands and saltmarshes also have significant heterogeneity in the belowground
86 organic phase: the structure and 3D deployment of roots within the soil vary depending on the

87 vegetation type. Furthermore, the roots' internal structure and density depend on their stage of
88 decay, which complicates the differentiation of live roots, necromass and pore space.

89 Significant advancements have been made to address the challenge of μ CT image segmentation
90 applied to heterogenous substrates, using more sophisticated "local adaptive" image processing
91 approaches such as gradient analysis and local-adaptive thresholding (Houston et al., 2013;
92 Ngom et al., 2011; Pot et al., 2020; Schlüter et al., 2010; Tarplee et al., 2011). Automated root
93 tracking algorithms have been developed to limit detection errors linked to the partial volume
94 effect ; however, they only detect root systems connected to the surface by user-specified seed
95 points, and might therefore miss buried root systems, which is a problem for soil carbon studies.
96 Another approach is to detect phase elements based on their 3D shapes rather than their
97 grayscale value, such as the tubular shape of roots using a Frangi filter (Frangi et al., 1998; Gao
98 et al., 2019; Schulz et al., 2013). These recent root detection methods give promising results, but
99 have so far been tested on sieved and repacked soils (Gao et al., 2019; Lucas et al., 2019), thus
100 eliminating the structural complexity of in situ soil systems and limiting our insight into soil
101 functions.

102 This study presents and evaluates a workflow for segmenting pores and organic phases in
103 complex heterogeneous, saturated sediment such as those found in coastal saltmarshes. Our
104 segmentation approach allows the user to quantify the interactions and complexity of both pores
105 and organic matter elements, and to distinguish the surface-connected live roots from the
106 necromass in order to get a complete picture of material interactions in heterogeneous soils. We
107 will discuss the potential applications of this approach to the study of key soil functions, such as
108 soil-plant interactions, soil structural stability against eroding forces, and soil carbon dynamics.

109

110 2. Methods

111

112 2.1. Study site

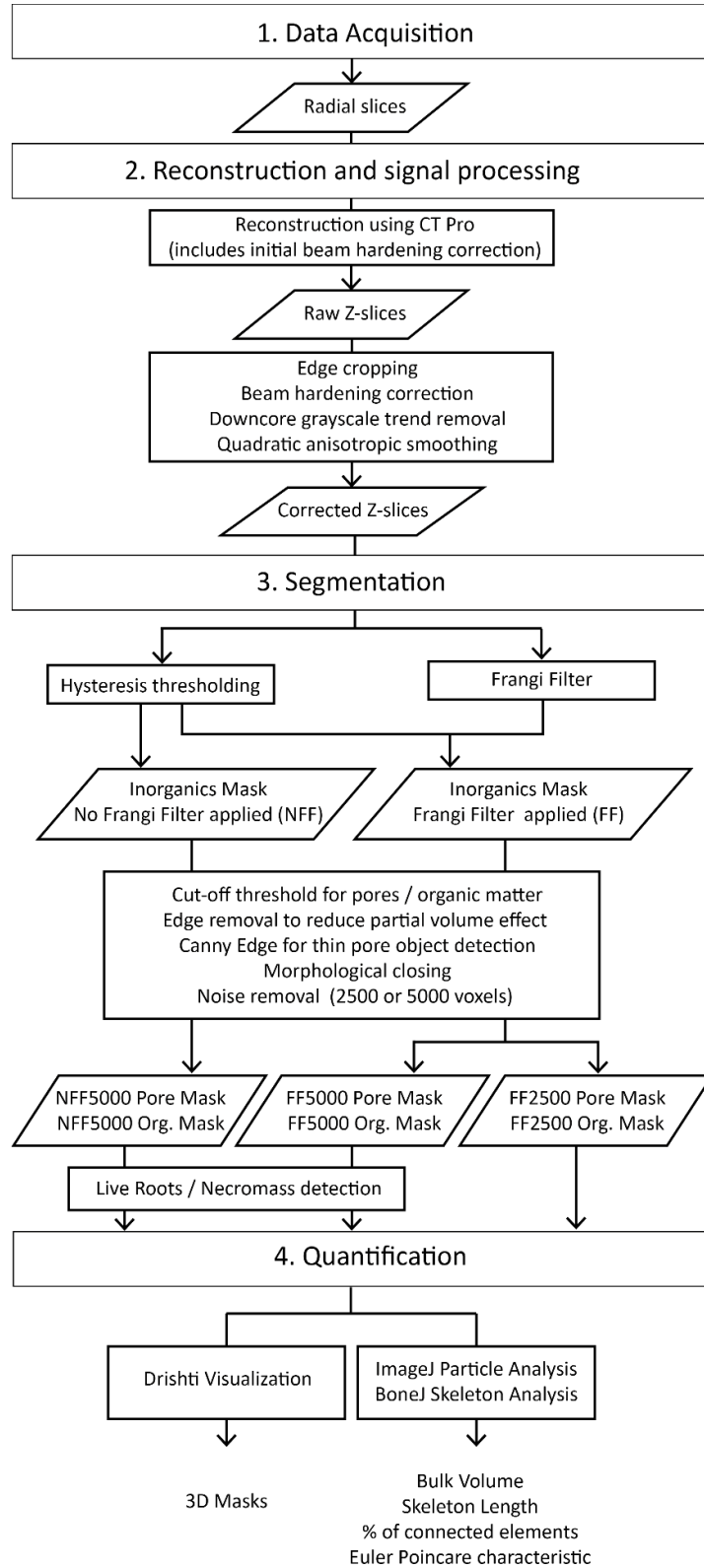
113 The site chosen to conduct this study, a saltmarsh in Tillingham, Blackwater Estuary, Essex, UK,
114 is representative of the heterogenous environments described above. Saltmarsh sediments are
115 typically formed of mixed fine-grained sediments (clays to medium sands) and biogenic
116 material, which makes them easily compacted and deformed during extraction. While
117 saltmarshes have a low vegetation diversity compared to nearby non-saline environments
118 (Teixeira et al., 2014), they are highly complex: tidal hydrology and strong vertical
119 physicochemical gradients mean that water content, plant survival rates, root to shoot ratio and
120 biomass accumulation vary in space and time (Moffett et al., 2012; Pezeshki & DeLaune, 2012).
121 In addition, the saltmarsh subsurface structure depends on tidally controlled sediment deposition,
122 but also on post-deposition processes such as autocompaction, bioturbation and root growth (De
123 Battisti et al., 2019; French, 2006; Turner, 2004). These characteristics mean that saltmarsh soils
124 are excellent candidates to test the robustness of our μ CT segmentation methods on challenging,
125 highly heterogeneous samples.

126 An upper saltmarsh sediment core (15 cm depth and 15 cm diameter) was collected in July 2018.

127 The vegetation cover at the sample location is dominated by *Atriplex portulacoides* (sea
128 purslane), *Puccinellia maritima* and *Spartina anglica* (Ford et al., 2016). The sediment type is
129 clay-dominated with a mean grain size of $69 \mu\text{m}$, with 71% of its material below $63 \mu\text{m}$. The
130 sediment core was collected using the advanced trimming method initially developed by
131 Hvorslev (1949): in brief, a plastic tube is placed on the soil surface; a trench is cut around the

132 tube, then carved into the shape of the core while the tube is lowered around the sample,
133 applying gentle constant pressure to limit edge drag and avoid compression and torque rotation.
134 Large roots are cut with scissors rather than a knife to avoid jostling, impact, twisting or other
135 deformation to the sediment inside the core. Fine fibrous roots are sawed through with a serrated
136 knife to avoid crushing and displacing the sediment around them. Further details and
137 justifications for the sampling method are provided by Carr et al. (2020). After extraction, the
138 core was stored upright in a cooling box filled with bubble wrap to minimize disturbance during
139 transport, and stored at 4 °C until required.

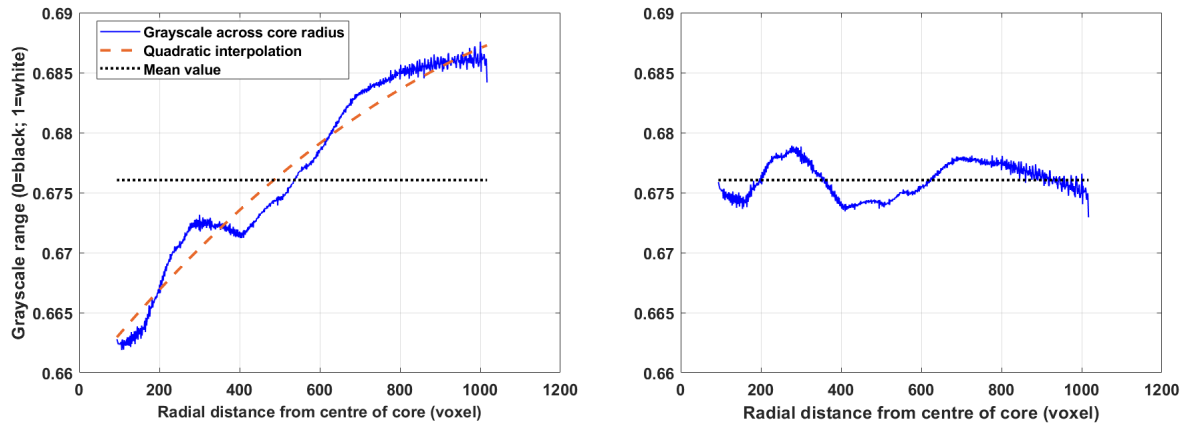
140 The core was scanned using a Nikon Metrology XT H 225 X-ray Computed Tomography (μ CT)
141 system at 205kV and 46μ A (9.4 W). The exposure time was 500ms at 36 dB gain. A Cu 1mm
142 copper filter was used to reduce beam hardening artefacts. 4486 projections were acquired with 4
143 frames per projection, for a scan time of 4.5 hours. The effective voxel size is 61.79μ m. The
144 voxel grid was then downscaled to 62.5μ m during volume reconstruction. The total volume
145 contains $2801*2783*2793$ voxels. Figure 1 summarizes the various steps applied to the scanned
146 volume. The different steps following scanning are detailed in the subsections below.



148 **Figure 1.** Data acquisition and processing workflow. The overall processing time from scanning
149 to obtention of output parameters is about four days on a high performance computing suite.

150 **2.2.Reconstruction and signal processing**

151 The volume reconstruction step was undertaken using Nikon's in-house software CT-Pro 3D
152 (Ray, 2011): the software finds the center of rotation of the raw X-ray projections and converts
153 the 2D radial slices into a 3D volumetric model defined by co-registered z-slices. The software
154 also partially corrects the z-slices for beam hardening using a polynomial fit: this imaging
155 artefact occurs when the X-ray beam becomes progressively attenuated as it penetrates from the
156 edge to the center of the sample, leading to an apparent darkening of the center and a brightening
157 of the edges (Ketcham & Carlson, 2001). This type of correction works when the overall matrix
158 can reasonably be assumed to have a consistent density throughout the sample (Ketcham &
159 Carlson, 2001), which should be the case for our clay-dominated material. Residual beam
160 hardening can still affect the segmentation phase, even when invisible to the naked eye. To
161 minimize its impact while removing edge disturbances during field sampling, an 8.75*8.75 cm
162 square mask was selected in the center of each z-slice as an area of interest and applied
163 throughout the volume (Fig. 1). A quadratic correction was then applied to the mean radial
164 grayscale, the grayscale value averaged vertically across the core and plotted against the radial
165 distance from the center (Fig. 2).



166

167

Figure 2. Correction of the residual beam hardening using a quadratic interpolation to remove

168

the overall trend of darker values at the center of the sample. The density variations that remain

169

in the detrended grayscale range correspond to actual density variations in the sample.

170

Compared to other soils where the material density is consistent throughout, another challenge of

171

clay-dominated coastal sediment is that they are highly compressible and may have rapid

172

sedimentation rates due to material brought in by the tide (French, 2006), leading to

173

autocompaction and to a downcore increase in the density of the inorganic phase. In our sample,

174

a linear trend in grayscale values is found with an R^2 value of 0.75 (Fig. 3); a lack of a similar

175

trend in the PVC tube around the sample (not shown) confirms that this trend is due to

176

autocompaction rather than an artefact of scanning. In order to more consistently distinguish the

177

mineral phase from the porosity and organic matter, this downcore trend is removed using a

178

linear interpolation (Fig. 3). In practice, this means smoothing out the microporosity through the

179

sample, which decreases with depth and affects the grayscale value of inorganic voxels due to

180

the partial volume effect. A shift remains at the top few centimeters of the sample, where the

181

trend is closer to a logarithmic fit in accordance with autocompaction patterns measured in silty

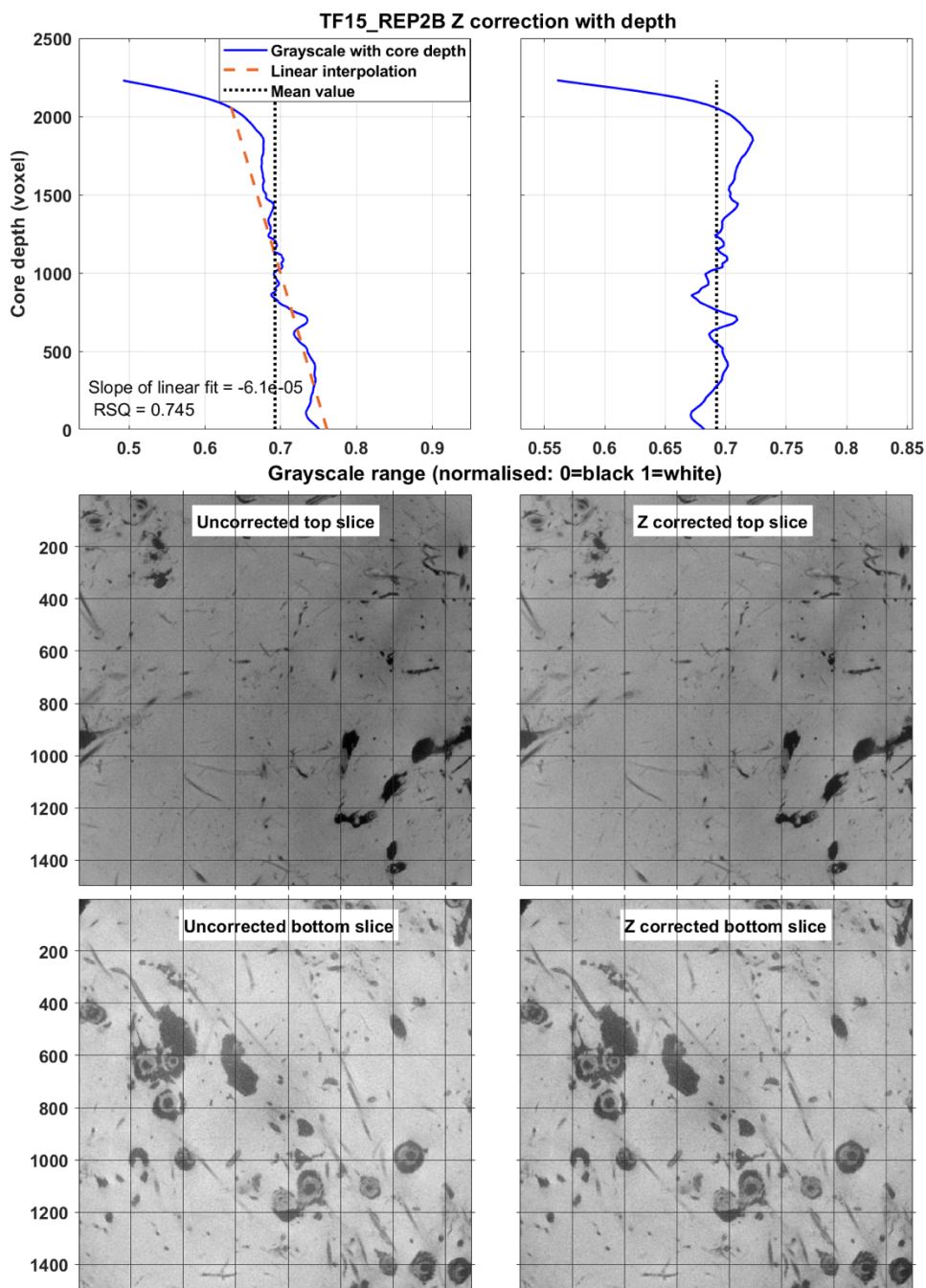
182

saltmarsh clay (Bartholdy et al., 2010). However, applying a logarithmic correction to the

183

topmost centimeters of the sample would excessively distort the grayscale value of the pores and

184 organic matter, which we can expect to find in greater quantity near the surface. This step
185 improves the segmentation of pores and roots in compressible sediment and soils, which is the
186 focus of this paper; however, analysis of the sediment phase should use the unmodified grayscale
187 values.



188

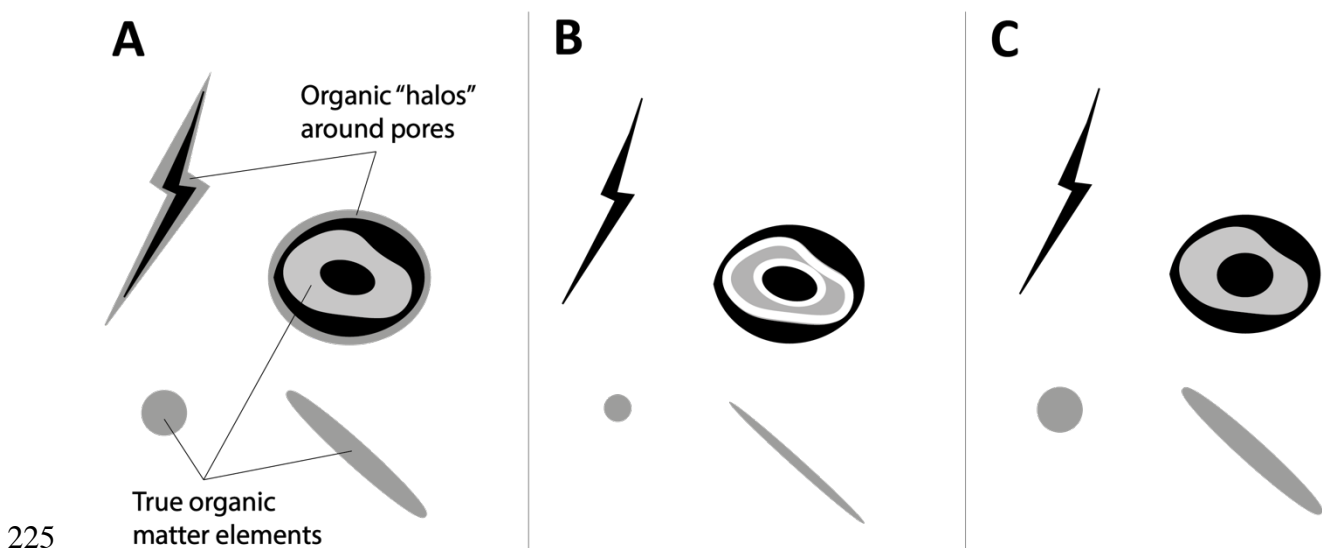
189 **Figure 3.** Removal of the autocompaction effect on grayscales using a downcore linear fit. The
190 correction factor at each z-slice is given by subtracting the linear fit from the uncorrected mean
191 grayscale then adding the mean grayscale of the whole core. The method does not remove the
192 logarithmic trend at the top of the sample so as to not excessively distort the grayscale values of
193 the pores and organic matter.

194 Finally, in order to reduce noise in the grayscale values while preserving the edges of the pores
195 and organic features, different smoothing algorithms were tested using image filtering tools on
196 Matlab, including Gaussian 3D filtering, 3D median filtering, guided image filtering and
197 anisotropic diffusion (quadratic and exponential). The quadratic anisotropic diffusion tool
198 *imdiffusefilt* was found to be best suited for filtering out noise without losing the signal: the
199 method enhances the contrast between matrix and darker elements by using strong gradients in
200 the image as barriers to the smoothing effect and thus preserving the edges (Kaestner et al.,
201 2006).

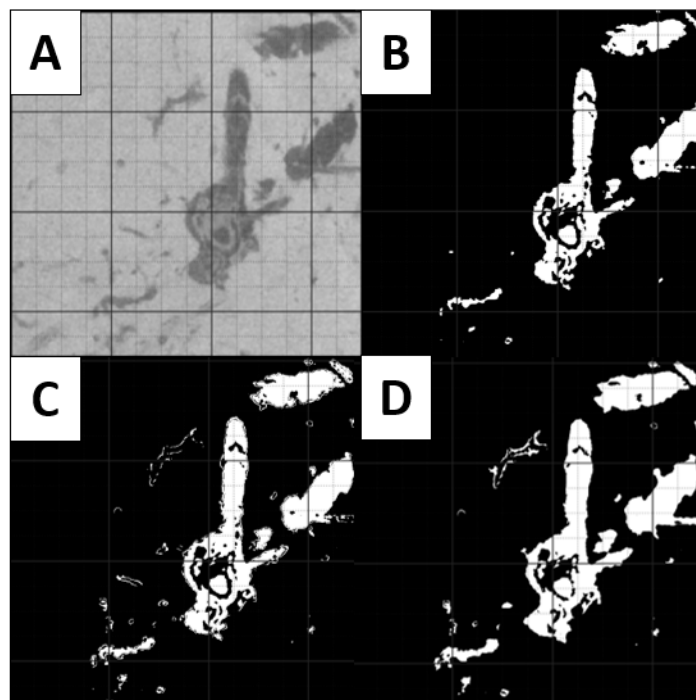
202 2.3.Segmentation

203 As stated in the introduction, μ CT data applied to heterogeneous fine grained substrates are
204 challenging to segment into their constituting phases because the partial volume effect blurs the
205 limit between phases (Cnudde and Boone, 2013), and are better served by a combination of local
206 adaptive thresholding methods. We first applied a method called hysteresis thresholding to
207 distinguish the high-density inorganics from pores and organic matter. This method considers
208 two thresholds: voxels below the low threshold have a high likelihood of being part of a pore or
209 organic element and are systematically segmented, while voxels below the high threshold are
210 only segmented if they are connected to the low threshold elements. A Frangi filter was then

211 used to enhance tubular shapes within the sample by applying the Matlab function
212 *FrangiFilter3D* (Kroon, 2010). The Frangi method uses the orientation patterns (eigenvalues) of
213 the Hessian to distinguish tubular structures from plate-like or blob-like structures (Frangi et al.,
214 1998). The output binary masks from hysteresis thresholding and Frangi tubular shape
215 enhancement were combined, adopting a single threshold to separate pores from organic matter.
216 Additional steps were then added to improve the signal to noise ratio, including morphological
217 closing and the removal of partial volume effect artefacts, which can lead to the detection of
218 organic “halos” around pore elements. The outer edges of organic matter elements were
219 removed, then a dilation was performed to restore the remaining organic features to their original
220 size (Fig. 4). Finally, in the same way that root elements can have a low contrast with the
221 surrounding inorganic matrix but a characteristic tubular shape, thin cracks in the sediment can
222 have an intermediate grayscale value due to the partial volume effect, but a visible jagged edge.
223 To capture these remaining pore elements, we used a canny edge detection that detects both
224 strong edges and weak edges connected to strong edges (Canny, 1986) (Fig. 5).



226 **Figure 4.** Schematic diagram illustrating partial volume effect reduction using contour removal
227 (Matlab tool *bwmorph3*) followed by dilation (Matlab tool *imdilate*). Grey: Organic matter
228 elements. Black: Pores. A: Initial segmentation of pores and organic matter elements; the partial
229 volume effect causes organic “halos” to be detected around the pore elements. B: Remove edges
230 of the organic phase to erase “halos” from partial volume effect. C: Dilate remaining organic
231 matter elements back to their original size.



232

233 **Figure 5.** Application of a Canny edge filter to refine pore detection in the sample. A: Original
234 grayscale values. B: Pore segmentation without the Canny edge detection. C: Canny edge
235 detection applied to find the edges of pore elements (Young, 2014); notice how the canny edges
236 do not always connect with the features from B and add internal complexity to the pore phase. D:
237 Morphological closing applied to reconnect the pore features to their edges (Matlab tool
238 *imclose*).

239 In order to remove the noise detected by these various methods, we tested two noise thresholds:
240 2,500 voxels (0.61 mm³) and 5,000 voxels (1.22 mm³) (FF2500 and FF5000 respectively).
241 FF2500 contains 7,066 organic matter elements compared to 4,106 for FF5000 according to the
242 Matlab volumetric image processing function *bwconncomp*; this will significantly increase the
243 computational intensity of the quantification phase. Through visual comparison of the 3D
244 volumes for FF5000 and FF2500, and quantitative comparison of the percentages of pore and
245 organic fractions with depth, we tested whether this lower threshold significantly improves
246 signal detection, or whether the additional ~3,000 elements detected are noise elements with
247 little impact on the structure of the organic matter phase. We also tested whether the application
248 of a Frangi filter, which takes several hours to run, significantly changes the detection of the live
249 roots and necromass. To that end, a third version of the dataset NFF5000 was produced, using all
250 the previous steps except for the Frangi filter, and using a noise removal threshold of 5,000
251 voxels.

252 Traditional methods for distinguishing live from dead roots are based on color, shape and
253 plasticity ADDIN CSL_CITATION {"citationItems":[{"id":"ITEM-
254 1","itemData":{"DOI":"10.1155/2012/217402","author":[{"dropping-
255 particle":"","family":"Persson","given":"Hans A","non-dropping-particle":"","parse-
256 names":false,"suffix":""}], "container-title":"International Journal ofForestry
257 Research","id":"ITEM-1","issued":{"date-parts":[["2012"]]}, "title":"The High Input of Soil
258 Organic Matter from Dead Tree Fine Roots into the Forest Soil","type":"article-
259 journal","volume":"2012"},"uris":["http://www.mendeley.com/documents/?uuid=4ccc3ad8-
260 7479-4f71-9f36-c206758f38fd"]}], "mendeley":{"formattedCitation":"(Persson,
261 2012)","plainTextFormattedCitation":"(Persson,

262 2012)},"properties":{"noteIndex":0},"schema":"https://github.com/citation-style-
 263 language/schema/raw/master/csl-citation.json"}(Persson, 2012). However, color and plasticity
 264 are not visible in μ CT images, and while live roots tend to be larger and better branched than
 265 dead roots, densely grouped dead roots may be detected as one large, complex connected system;
 266 using these traditional definitions would therefore be prone to errors. Instead, in the binary masks
 267 NFF5000 and FF5000, we defined the live root system as all elements connected to the surface
 268 layer, approximated by the top 80 voxels (= 5mm) of the sample. The remaining, unconnected
 269 elements were classified as necromass.

270 2.4. Quantification and ground referencing

271 The 3D binary masks NFF5000, FF5000 and FF2500 were used for a detailed topological
 272 analysis of the pores and organic matter elements using the automated software plugin BoneJ for
 273 ImageJ (Doube et al., 2010; Schindelin et al., 2012). Morphological parameters (Table 2) were
 274 extracted to determine how the different segmentation approaches affect the volume, length and
 275 structural complexity of the pore and organic phases.

276 **Table 1.** List of morphological parameters considered.

Parameter	Unit	Definition
Total phase fraction	%	Fraction of the number of voxels belonging to a phase by the total number of voxels in each Z-slice and represented as depth profiles. The surface of the sample is automatically detected as the Z-slice wherein the proportion of matrix to void, segmented using an Otsu global thresholding, first reaches 75%.
Total volume	mm ³	Total volume of the studied phase
Total skeleton length	mm	Total length of the skeleton, obtained by shrinking a volume to a 1-voxel thick median structure, composed of nodes and branches that preserve the topological complexity of the initial volume.

Connectedness	%	Volume of the largest connected element divided by the total volume of the studied phase
Maximum Euler-Poincare characteristic	No unit	Topological invariant that describes the shape or structure of a topological space. In BoneJ, it is calculated as the number of objects minus the number of handles (hole that goes through an object) plus the number of cavities (holes enclosed within the object). It is used as a proxy for complexity and connectedness: negative values correspond to a well-connected complex system.

277

278 The 3D architecture of the sample was visualized using the volume rendering software Drishti
 279 (Limaye, 2012). In order to compare this 3D rendering with the actual sample, and check that the
 280 root and pore elements visible to the naked eye are correctly identified, the core was cut open
 281 with a serrated knife along a pre-marked section one day after scanning. Using a prior marking
 282 (either an incision in the PVC tube or a piece of metal, both of which will be visible in the X-ray
 283 attenuation coefficients), the equivalent vertical section was located in the segmented volume
 284 and overlain with a high-resolution photograph of the cut-off face. While there is no infallible
 285 way of cutting open a core without causing disturbance, the cohesive nature of the clay means
 286 that the largest pore structures and the position of the roots are likely to be preserved.

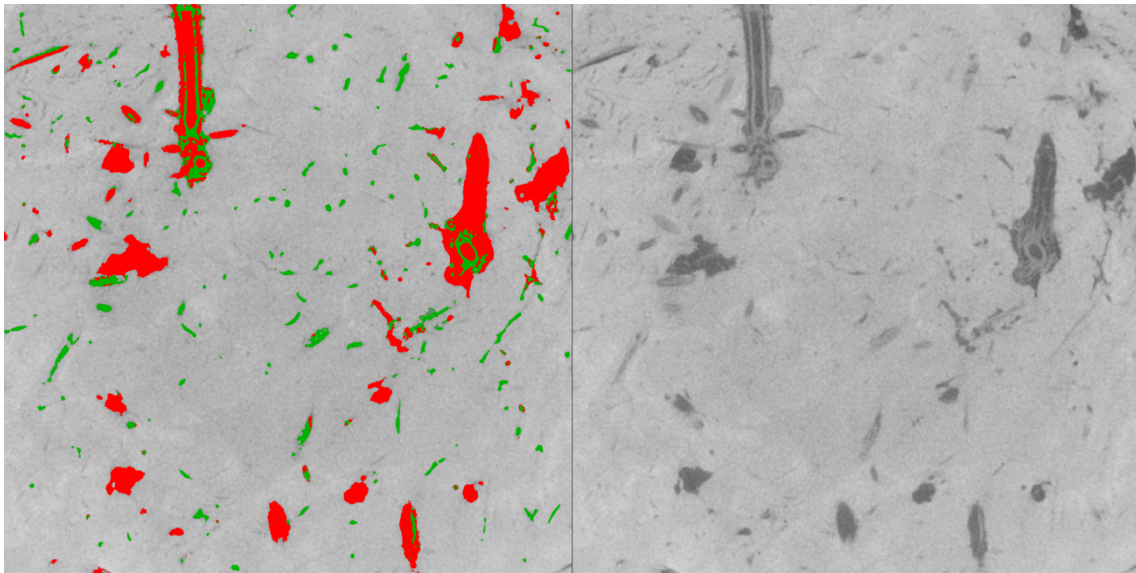
287 **3. Results**

288

289 **3.1. Quality control of the segmentation method**

290 Observation of the segmented horizontal slices provides insight into the different types of pores
 291 and organic matter elements detected by our segmentation method (Fig. 6). The larger organic
 292 elements have a complex inner structure with a hollow center and multiple other internal voids:
 293 these air spaces within roots and stems (aerenchyma) are an adaptation strategy of coastal
 294 wetland plants such as *Spartina* to anoxic conditions (Mitsch & Gosselink, 1986). The smaller,

295 tubular root elements visible in the Z-slice correspond either to lateral roots branching off from
296 the main *Spartina* root system, or to the roots of other plant species present on site such as
297 *Atriplex* or *Puccinellia*. The porosity elements appear either as tubular features, corresponding to
298 inner voids within roots and voids left behind by decaying roots, or as patches with no organic
299 origin.

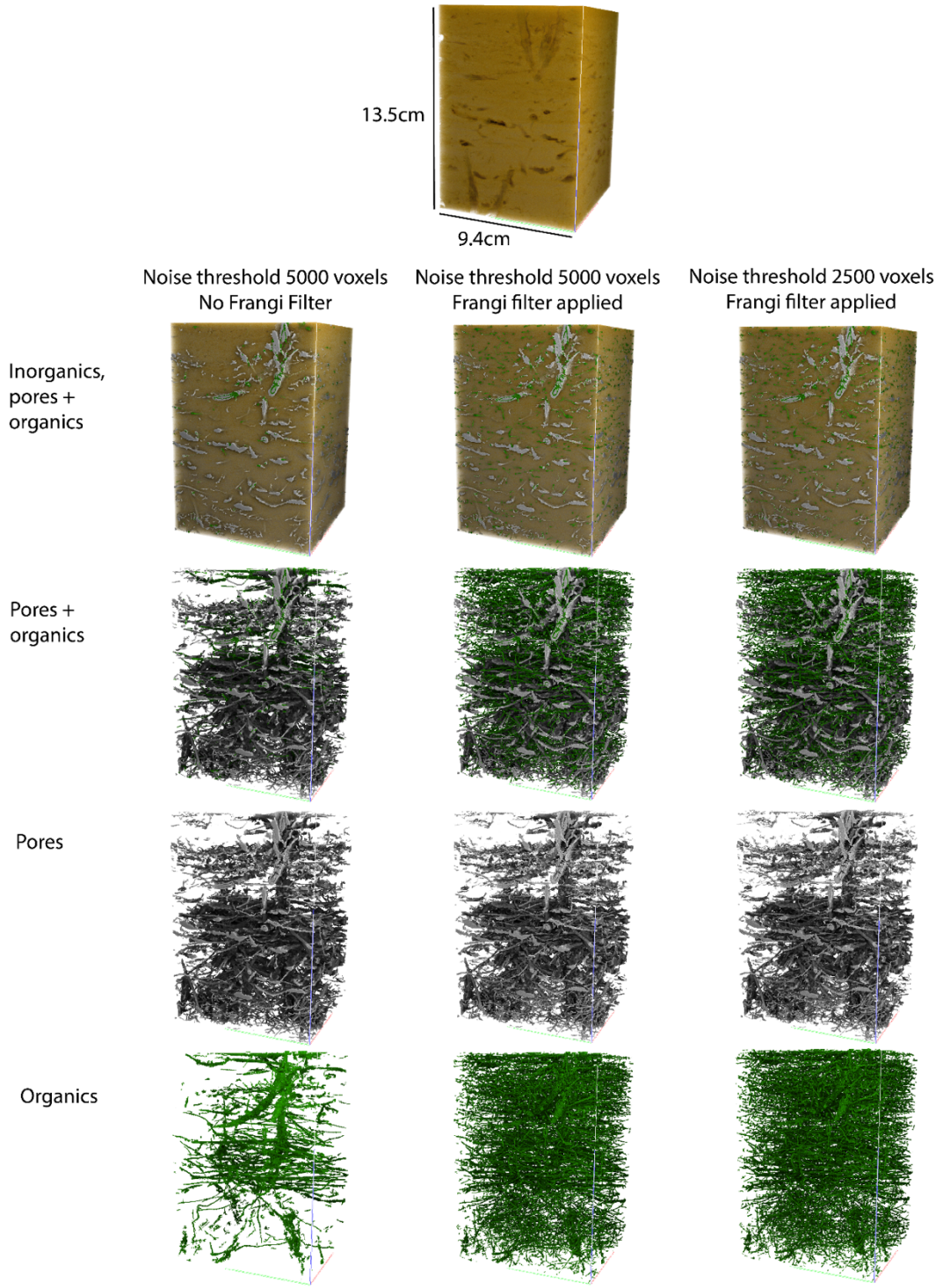


300

301 **Figure 6.** Segmentation example, showing the pore phase in red and the organic matter phase in
302 green overlain over the remaining inorganic phase.

303 Adding the Frangi filter had no visible effect on the detection of pore elements, but considerably
304 increased the size, extent and complexity of the organic matter phase (Fig. 7). At NFF5000 the
305 organic matter phase is limited to areas connected to large pores: because of the hysteresis
306 thresholding applied, medium grayscale voxels are only segmented if they are connected to a low
307 grayscale voxel. Therefore the Frangi filter is particularly efficient at detecting thin unconnected
308 root elements with no internal voids. By contrast, changing the noise removal threshold from

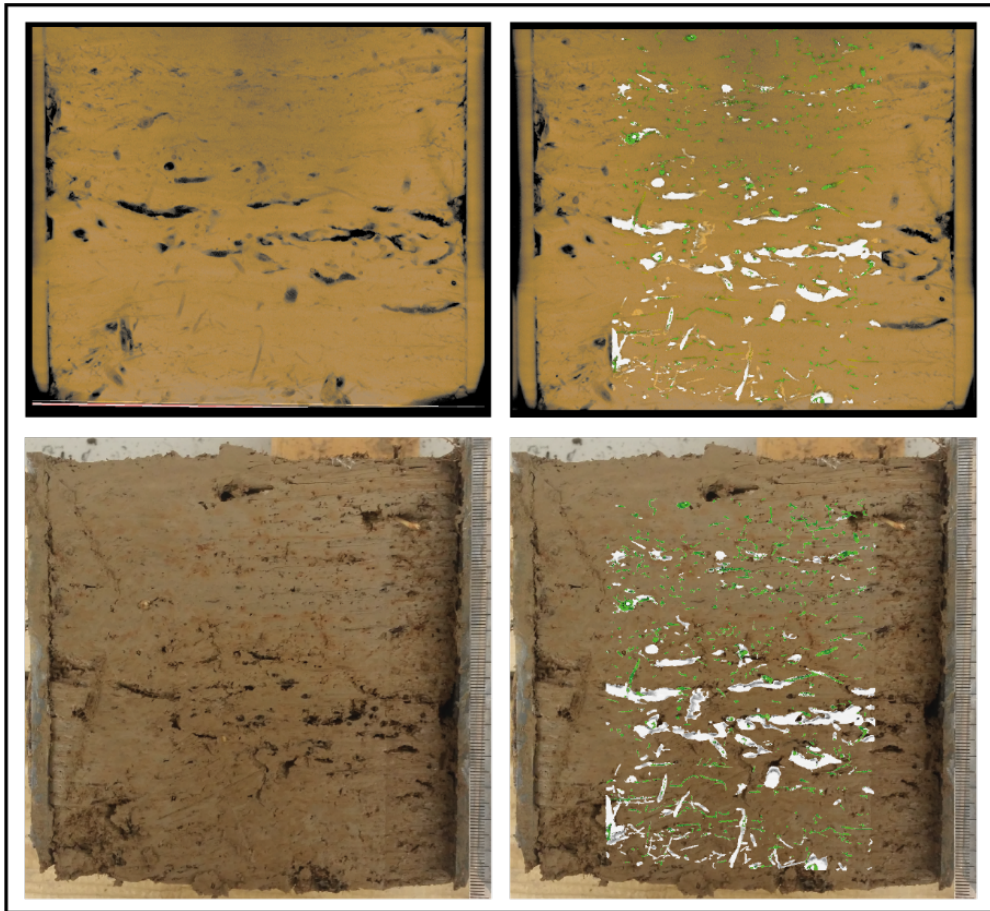
309 5,000 to 2,500 voxels had little visible impact on the 3D volumes of either the pore or the
310 organic matter phases (Fig. 7).



311

312 **Figure 7.** Segmented volume visualization using different segmentation methods and noise
313 thresholds. Grey = pores; green = organic matter; brown = inorganic matter. Volumes obtained
314 using Drishti (Limaye, 2012).

315 Ground referencing shows that the segmentation method proposed successfully distinguishes
316 areas dominated by roots from areas dominated by pores (Fig. 8). On the high resolution
317 photograph, the top half of the cut face (0-6 cm) is pockmarked by small roots, though individual
318 roots are difficult to visualize except for a few of the larger *Spartina* roots. The section between
319 6-12 cm contains more and larger porosity elements; the structure and distribution of these pores
320 are also similar to what is observed on the segmented volume.



321

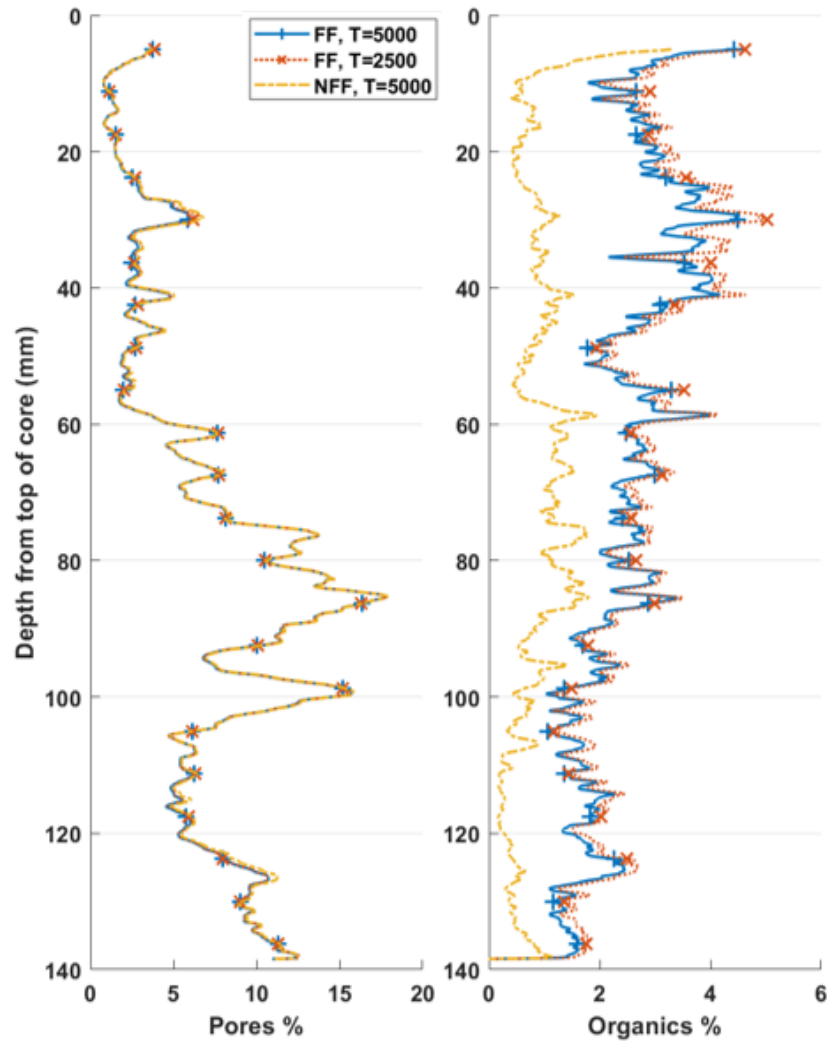
322 **Figure 8.** Ground referencing using the segmented volume overlain over a photograph of the
323 cut-off face of the core. On the segmented volume: brown = inorganic matter; grey = pores;
324 green = organic matter. Volume obtained using Drishti.

325 3.2. Quantification and distinction between live roots and necromass

326 The segmented pore phase can be separated into three regions: 0-6 cm, 6-10 cm and 10-14 cm.
327 The first region at 0-6 cm is characterized by a low pore fraction and bulk volume, a low
328 connectivity, but a peak in both the pores and organic matter' skeleton length (Fig. 9-10). This is
329 due to the influence of the *Spartina* stem and roots, which contain several transport pathways and
330 unconnected hollow chambers that add to the length of the overall pore system. The second
331 region at 6-10 cm sees a peak in the pore fraction (Fig. 9) and in the connectedness and
332 complexity of the pore system (Fig. 10). This region coincides with the branching off of the main
333 *Spartina* root into lateral roots at about 8 cm, and with a horizontal crack visible in the rendered
334 volume (Fig. 7). The root system may have preferentially developed within an area of structural
335 fragility and lesser density, as has been observed in previous studies (Lucas et al., 2019). The
336 third region sees a slight decrease in the bulk volume, connectedness and complexity of the pore
337 system (Fig. 9-10).

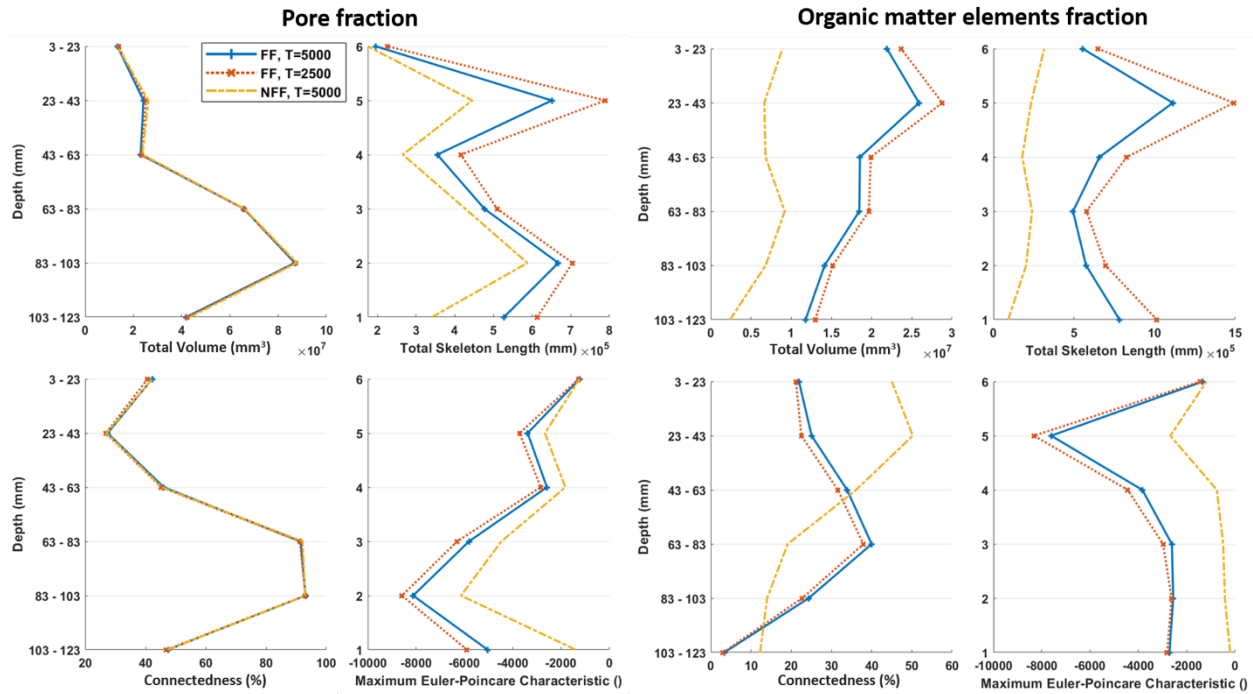
338 The organic matter phase is dense throughout the 15 cm sample (Fig. 7), which is to be expected
339 as we are still within the root zone of a biologically diverse upper saltmarsh: the saltmarsh root
340 zone extends from 15 to 50 cm depending on plant species and environmental conditions (De
341 Baets et al., 2008). The organic phase is denser in the first 5 centimeters then starts to decrease
342 downcore (Fig. 9). Adding the Frangi filter leads to the detection of a larger and more complex
343 organic matter phase overall, with a higher fraction, bulk volume and total skeleton length

344 detected at all depths (Fig. 9-10). Adding the Frangi filter also highlights the downcore decrease
345 of the organic fraction (Fig. 9), notably by detecting a higher number of elements not connected
346 to the main root system: in the first 5 cm of the sample, 25% of all segmented elements are
347 connected to the main root feature in FF5000 and FF2500, against 50% for NFF5000 (Fig. 10).



348

349 **Figure 9.** Depth profiles of the fractions of pores and of organic matter within the segmented
350 volume. FF: Frangi filter applied; NFF: No Frangi filter applied. T=5000: Noise threshold set at
351 5,000 voxels; T=2,500: Noise threshold set at 2,500 voxels.



352

353 **Figure 10.** Topological analysis of pores and organic matter in 2-cm sections using BoneJ. ()

354

stands for no unit.

355 Figure 11 shows the potential of the Frangi filter to detect the necromass as well as the surface-

356 connected live root system. The live root phase highlights one large *Spartina* root that branches

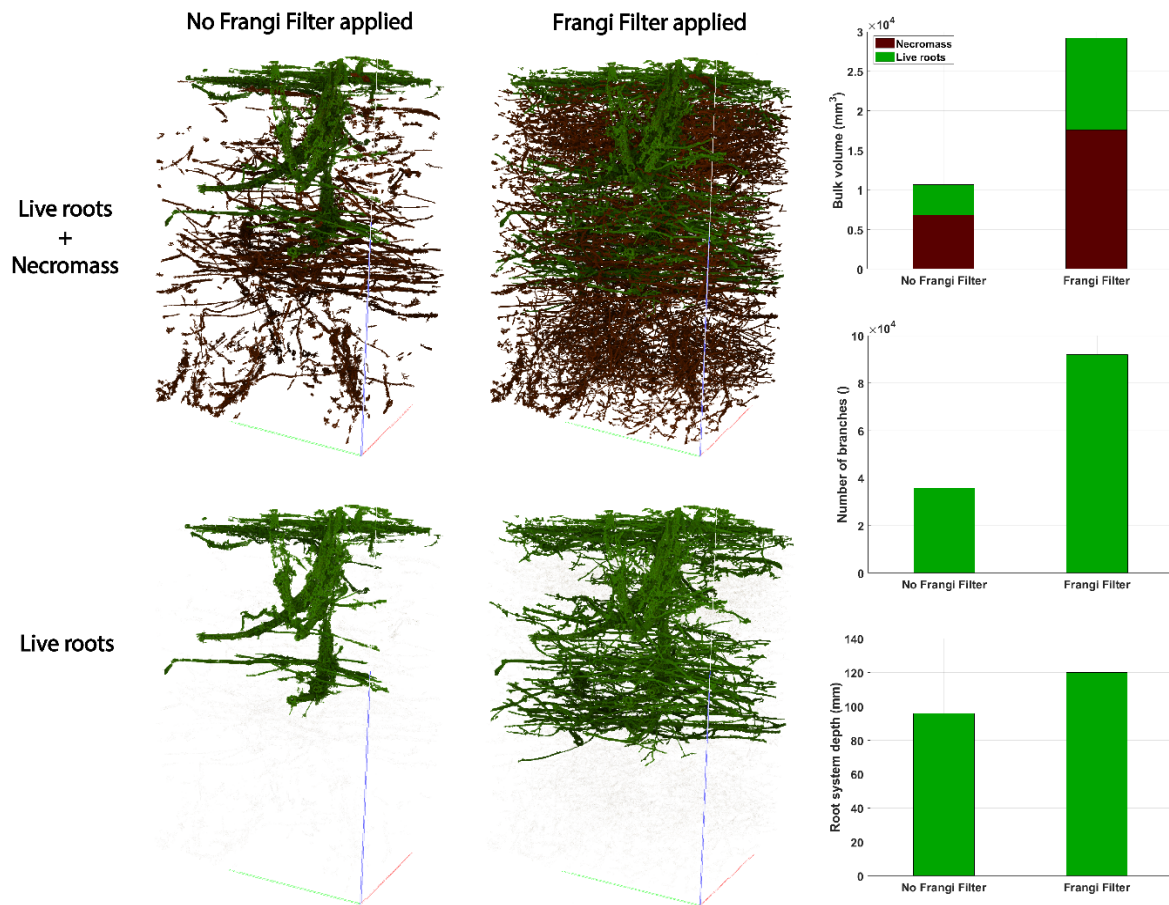
357 out into smaller horizontal roots at about 80 mm depth. The live root system detected using the

358 Frangi filter is larger and more complex, with a greater bulk volume and number of branches in

359 the skeleton, and reaches 2.5cm deeper. A number of thin lateral roots also becomes apparent.

360 Without the Frangi filter, by contrast, the live root system appears fragmented, and very little of

361 the necromass is detected.



362

363 **Figure 11.** Effect of the Frangi filter on the extent, bulk volume, number of branches and root
 364 system depth of surface-connected “live” roots (green) and on the bulk volume of the necromass
 365 (dark red). The noise threshold is 5000 voxels.

366 4. Discussion

367 The use of μ CT in soil sciences allows us to visualize and quantify crucial structures and
 368 processes in the subsurface environment, but this technology presents ongoing challenges:
 369 sampling procedures to minimize sediment disturbance remain time-consuming, access to
 370 specialist X-ray μ CT scanning equipment is still not widespread in the soil science community,
 371 and the large datasets can create issues with processing and data storage. Finally, until standard

372 segmentation methods are widely agreed upon, interpretation of the μ CT volumes will require
373 specific expertise in 3D signal processing and image analysis. Therefore multidisciplinary
374 methodology papers are necessary to disseminate novel image processing techniques and
375 encourage the wider use of μ CT by soil scientists.

376 The approach outlined in this paper has multiple potential applications for soil science. The
377 three-phase segmentation (pores, organic matter elements, sediment matrix) allows the study of
378 pore-root interactions, something which has so far only been attempted in simplified conditions
379 such as sieved and repacked soil columns (Lucas et al., 2019). These interactions are expected to
380 play an important role in natural soil structure because of the high trait plasticity of roots: their
381 growth depends on the distribution of water, nutrients and of the areas of least resistance marked
382 by the porosity elements (Bardgett et al., 2014). At a higher resolution, the method could be used
383 to study the internal structure of plants and roots to visualize internal air spaces and infer nutrient
384 and fluid exchanges between the surface and subsurface: the presence of aerenchyma has been an
385 obstacle in previous segmentation attempts using a visual tracking algorithm . In addition, the
386 capacity of our method to distinguish live roots from the necromass opens the door for μ CT
387 applications to the study of soil structural stability. Indeed, roots can have either a weakening or
388 a stabilizing effect on the soil depending on their structure, connectedness and state of decay
389 (Brooks et al., 2020). Coarse roots can dislodge sediment and contribute to cliff-face erosion
390 (Feagin et al., 2009), while thinner and denser root meshes hold the soil together and provide a
391 physical barrier between the sediment and the water (Brooks et al., 2020; Gedan et al., 2011).
392 Decaying unconnected roots also contribute to making the soil less dense and more cohesive
393 (Brooks et al., 2020; Feagin et al., 2009).

394 Finally, the proposed method opens the door to the study of soil carbon dynamics and
395 greenhouse gas exchanges in various types of soils. The potential of μ CT to model gas
396 exchanges within 3D macropore structures is already known (van Marcke et al., 2010). Our
397 approach can further the state of knowledge by providing a robust way of estimating root
398 biomass. This should improve the estimation of carbon stocks since root systems and particularly
399 the fine-root mass contribute disproportionately to soil carbon sequestration compared to the
400 aboveground part of the plant (He et al., 2018). Root biomass estimation still lacks a
401 methodological consensus (Addo-Danso et al., 2016), and traditional methods of belowground
402 biomass estimation rely on labor-intensive and time-consuming destructive sampling protocols,
403 as highlighted by Vialiale (2015): “This project became legendary as the most tedious task in our
404 labs, tolerated only by everyone taking turns at the detailed and nearly endless staining, sorting,
405 drying, and weighing protocols”. Furthermore, distinguishing live roots from necromass is
406 recommended when estimating carbon sequestration potential in the soil (Adame et al., 2017).
407 The proposed method, based on the connection of the root system to the surface, comes with its
408 own limitations: the minimal size of roots detected depends on the scanning resolution chosen,
409 and live root systems connected to shoots outside the perimeter of the core will be detected as
410 necromass; prior knowledge of the live root thickness, internal structure and architecture is
411 recommended to choose appropriate scanning parameters and to interpret the μ CT volumes.
412 Nevertheless, owing to the capacity of μ CT to rapidly and non-destructively segment large and
413 complex root systems, the method outlined in this paper could play a crucial role in studies of
414 soil carbon dynamics.

415 **5. Conclusion**

416 This study applied X-ray Computed Microtomography to a highly heterogenous saltmarsh
417 sediment core. We developed a hybrid segmentation method that combines local adaptive
418 thresholding and shape detection to visualize and quantify the 3D distribution of pores, live roots
419 and necromass. The segmented volumes of roots and pores closely match the structures observed
420 on high-resolution photographs of the core taken along a cut-off face. We find that the use of a
421 Frangi filter for tubular structure enhancement is particularly efficient to highlight fine root
422 elements that have a low density contrast with the mineral phase. Compared with region-growth
423 segmentation methods, which only segment objects connected to pre-selected seed points, this
424 method is more versatile because it requires no prior knowledge of the core content, and because
425 it distinguishes between the live root system and the necromass. Our analysis of the pore and
426 organic matter elements' volume and structure shows clear interactions between the two phases:
427 root decay is a source of porosity in the sediment, while the presence of areas of lower density
428 with a higher concentration of pores determine where roots are able to develop. Our application
429 of X-ray μ CT has the potential to provide unprecedented knowledge of the 3D organisation of
430 pores and organic matter within heterogeneous soils, and to explore key ecosystem functioning
431 such as erodibility and carbon sequestration dynamics.

432 **AUTHOR INFORMATION**

433 **Corresponding Author**

434 Clementine Chiról – Queen Mary University of London, School of Geography, E1 4NS, London,
435 UK. orcid; Email: clementine.chir@gmail.com

436 **Authors**

437 Simon Carr – University of Cumbria, Institute of Science, Natural Resources and Outdoor
438 Studies, LA22 9BB, Ambleside, Cumbria, UK. ORCID. Email: simon.carr@cumbria.ac.uk

439 Iris Moeller – Trinity College Dublin, School of Geography, Dublin 2, Ireland. ORCID. Email:
440 moelleri@tcd.ie

441 Kate Spencer – Queen Mary University London, School of Geography, E1 4NS, London, UK.
442 ORCID; Email: k.spencer@qmul.ac.uk

443 **Author Contributions**

444 The manuscript was written through contributions of all authors. All authors have given approval
445 to the final version of the manuscript. Iris Moeller secured funding for the RESIST project and
446 defined our research objectives. Kate Spencer and Simon Carr developed an initial workflow for
447 X-ray μ CT application to saltmarsh soils. Clementine Chirol collected the sample with field
448 assistance from all authors, processed the dataset using an enhanced workflow and wrote the
449 article with edits from all authors.

450 **Notes**

451 The authors declare no competing financial interest.

452 **ACKNOWLEDGMENT**

453 We acknowledge funding from the National Environment Research Council (NERC) for the
454 research project RESIST(UK) (grant number XXX). We would like to thank the School of
455 Geography laboratory manager Michelle Day at Queen Mary University London for the use of
456 their Nikon Metrology XT H 225 X-ray Computed Tomography (μ CT) system.

457 **ABBREVIATIONS**

458 FF, frangi filter; NFF, no frangi filter; μ CT, computer microtomography

459 REFERENCES

460 Adame, M. F., Cherian, S., Reef, R., & Stewart-Koster, B. (2017). Mangrove root biomass and the
461 uncertainty of belowground carbon estimations. *Forest Ecology and Management*,
462 403(January 2018), 52–60. <https://doi.org/10.1016/j.foreco.2017.08.016>

463 Addo-Danso, S. D., Prescott, C. E., & Smith, A. R. (2016). Methods for estimating root biomass
464 and production in forest and woodland ecosystem carbon studies: A review. *Forest Ecology
465 and Management*, 359(September), 332–351. <https://doi.org/10.1016/j.foreco.2015.08.015>

466 Ball, B. C. (2013). Soil structure and greenhouse gas emissions: A synthesis of 20 years of
467 experimentation. *European Journal of Soil Science*, 64(3), 357–373.
468 <https://doi.org/10.1111/ejss.12013>

469 Bardgett, R. D., Mommer, L., & Vries, F. T. De. (2014). Going underground : root traits as drivers
470 of ecosystem processes. *Trends in Ecology & Evolution*, 29(12), 692–699.
471 <https://doi.org/10.1016/j.tree.2014.10.006>

472 Bartholdy, J., Pedersen, J. B. T., & Bartholdy, A. T. (2010). Autocompaction of shallow silty salt
473 marsh clay. *Sedimentary Geology*, 223(3–4), 310–319.
474 <https://doi.org/10.1016/j.sedgeo.2009.11.016>

475 Bendle, J. M., Palmer, A. P., & Carr, S. J. (2015). A comparison of micro-CT and thin section
476 analysis of Lateglacial glaciolacustrine varves from Glen Roy, Scotland. *Quaternary Science
477 Reviews*, 114, 61–77. <https://doi.org/10.1016/j.quascirev.2015.02.008>

478 Blagodatsky, S., & Smith, P. (2012). Soil physics meets soil biology: Towards better mechanistic
479 prediction of greenhouse gas emissions from soil. *Soil Biology and Biochemistry*, 47, 78–92.

480 <https://doi.org/10.1016/j.soilbio.2011.12.015>

481 Bradley, P., & Morris, J. (1990). Physical characteristics of salt marsh sediments: ecological
482 implications. *Marine Ecology Progress Series*, 61, 245–252.
483 <https://doi.org/10.3354/meps061245>

484 Brooks, H., Möller, I., Carr, S., Chirol, C., Christie, E., Evans, B., Spencer, K. L., Spencer, T., &
485 Royse, K. (2020). Resistance of salt marsh substrates to near-instantaneous hydrodynamic
486 forcing. *Earth Surface Processes and Landforms*. <https://doi.org/10.1002/esp.4912>

487 Canny, J. (1986). A Computational Approach to Edge Detection. *IEEE Transactions on Pattern*
488 *Analysis and Machine Intelligence*, PAMI-8(6), 679–698.
489 <https://doi.org/10.1109/ASICON.2011.6157287>

490 Carr, S., Diggens, L., & Spencer, K. (2019). There’s no such thing as “undisturbed” soil and
491 sediment sampling: sampler-induced deformation of salt-marsh sediments revealed by 3D x-
492 ray computed tomography. *Journal of Soils and Sediments*.

493 Cnudde, V., & Boone, M. N. (2013). High-resolution X-ray computed tomography in geosciences:
494 A review of the current technology and applications. *Earth-Science Reviews*, 123, 1–17.
495 <https://doi.org/10.1016/j.earscirev.2013.04.003>

496 Corenblit, D., Baas, A. C. W., Bornette, G., Darrozes, J., Delmotte, S., Francis, R. A., Gurnell, A.
497 M., Julien, F., Naiman, R. J., & Steiger, J. (2011). Earth-Science Reviews Feedbacks between
498 geomorphology and biota controlling Earth surface processes and landforms : A review of
499 foundation concepts and current understandings. *Earth Science Reviews*, 106(3–4), 307–331.
500 <https://doi.org/10.1016/j.earscirev.2011.03.002>

501 Dale, J., Cundy, A. B., Spencer, K. L., Carr, S. J., Croudace, I. W., Burgess, H. M., & Nash, D. J.
502 (2019). Sediment structure and physicochemical changes following tidal inundation at a large
503 open coast managed realignment site. *Science of the Total Environment*, 660, 1419–1432.
504 <https://doi.org/10.1016/j.scitotenv.2018.12.323>

505 De Baets, S., Poesen, J., Reubens, B., Wemans, K., De Baerdemaeker, J., & Muys, B. (2008). Root
506 tensile strength and root distribution of typical Mediterranean plant species and their
507 contribution to soil shear strength. *Plant and Soil*, 305(1–2), 207–226.
508 <https://doi.org/10.1007/s11104-008-9553-0>

509 De Battisti, D., Fowler, M. S., Jenkins, S. R., Skov, M. W., Rossi, M., Bouma, T. J., Neyland, P.
510 J., & Griffin, J. N. (2019). Intraspecific Root Trait Variability Along Environmental
511 Gradients Affects Salt Marsh Resistance to Lateral Erosion. *Frontiers in Ecology and*
512 *Evolution*, 7(May), 1–11. <https://doi.org/10.3389/fevo.2019.00150>

513 Doube, M., Kłosowski, M. M., Arganda-carreras, I., & Fabrice, P. (2010). UKPMC Funders Group
514 BoneJ: free and extensible bone image analysis in ImageJ. *Bone*, 47(6), 1076–1079.
515 <https://doi.org/10.1016/j.bone.2010.08.023>.BoneJ

516 Dyer, K. R. (1995). Sediment transport processes in estuaries. *Geomorphology and Sedimentology*
517 *of Estuaries. Developments in Sedimentology*, 53, 423–449.
518 [https://doi.org/http://dx.doi.org/10.1016/S0070-4571\(05\)80034-2](https://doi.org/http://dx.doi.org/10.1016/S0070-4571(05)80034-2)

519 Feagin, R. A., Lozada-Bernard, S. M., Ravens, T. M., Möller, I., Yeager, K. M., & Baird, A. H.
520 (2009). Does vegetation prevent wave erosion of salt marsh edges? *Proceedings of the*
521 *National Academy of Sciences of the United States of America*, 106(25), 10109–10113.

522 <https://doi.org/10.1073/pnas.09012971106>

523 Fonseca, J., O’Sullivan, C., Coop, M. R., & Lee, P. D. (2013). Quantifying the evolution of soil
524 fabric during shearing using scalar parameters. *Geotechnique*, 63(10), 818–829.
525 <https://doi.org/10.1680/geot.11.P.150>

526 Ford, H., Garbutt, A., & Skov, M. (2016). *Coastal Biodiversity and Ecosystem Service*
527 *Sustainability (CBESS) percentage cover of plant species on salt marsh sites at Morecambe*
528 *Bay and Essex*. [https://doi.org/https://doi.org/10.5285/90bdf4ff-03d9-4aa4-bcad-](https://doi.org/https://doi.org/10.5285/90bdf4ff-03d9-4aa4-bcad-5139863ab188)
529 [5139863ab188](https://doi.org/https://doi.org/10.5285/90bdf4ff-03d9-4aa4-bcad-5139863ab188)

530 Frangi, A. F., Niessen, W. J., Vincken, K. L., & Viergever, M. A. (1998). Multiscale vessel
531 enhancement filtering. *International Conference on Medical Image Computing and*
532 *Computer-Assisted Intervention*, 130–137. <https://doi.org/10.1007/BFb0056195>

533 French, J. (2006). Tidal marsh sedimentation and resilience to environmental change: Exploratory
534 modelling of tidal, sea-level and sediment supply forcing in predominantly allochthonous
535 systems. *Marine Geology*, 235(1-4 SPEC. ISS.), 119–136.
536 <https://doi.org/10.1016/j.margeo.2006.10.009>

537 Gao, W., Schlüter, S., Blaser, S. R. G. A., Shen, J., & Vetterlein, D. (2019). A shape-based method
538 for automatic and rapid segmentation of roots in soil from X-ray computed tomography
539 images: Routine. *Plant and Soil*, 441(1–2), 643–655. [https://doi.org/10.1007/s11104-019-](https://doi.org/10.1007/s11104-019-04053-6)
540 [04053-6](https://doi.org/10.1007/s11104-019-04053-6)

541 Gedan, K. B., Kirwan, M. L., Wolanski, E., Barbier, E. B., & Silliman, B. R. (2011). The present
542 and future role of coastal wetland vegetation in protecting shorelines: Answering recent

543 challenges to the paradigm. In *Climatic Change* (Vol. 106, Issue 1, pp. 7–29).
544 <https://doi.org/10.1007/s10584-010-0003-7>

545 Gharedaghlou, B., Price, J. S., Rezanezhad, F., & Quinton, W. L. (2018). Evaluating the hydraulic
546 and transport properties of peat soil using pore network modeling and X-ray micro computed
547 tomography. *Journal of Hydrology*, 561(September 2017), 494–508.
548 <https://doi.org/10.1016/j.jhydrol.2018.04.007>

549 Griggs, A. J., Davies, S. M., Abbott, P. M., Coleman, M., Palmer, A. P., Rasmussen, T. L., &
550 Johnston, R. (2015). Visualising tephra sedimentation processes in the marine environment:
551 The potential of X-ray microtomography. *Geochemistry, Geophysics, Geosystems*, 16, 4329–
552 4343. <https://doi.org/10.1002/2015GC006073>.Received

553 He, Z., Peng, Y., Guan, D., Hu, Z., Chen, Y., & Lee, S. Y. (2018). Appearance can be deceptive:
554 shrubby native mangrove species contributes more to soil carbon sequestration than fast-
555 growing exotic species. *Plant and Soil*, 432(1–2), 425–436. [https://doi.org/10.1007/s11104-](https://doi.org/10.1007/s11104-018-3821-4)
556 [018-3821-4](https://doi.org/10.1007/s11104-018-3821-4)

557 Helliwell, J. R., Sturrock, C. J., Grayling, K. M., Tracy, S. R., Flavel, R. J., Young, I. M., Whalley,
558 W. R., & Mooney, S. J. (2013). Applications of X-ray computed tomography for examining
559 biophysical interactions and structural development in soil systems: A review. *European*
560 *Journal of Soil Science*, 64(3), 279–297. <https://doi.org/10.1111/ejss.12028>

561 Houston, A. N., Schmidt, S., Tarquis, A. M., Otten, W., Baveye, P. C., & Hapca, S. M. (2013).
562 Effect of scanning and image reconstruction settings in X-ray computed microtomography
563 on quality and segmentation of 3D soil images. *Geoderma*, 207–208(1), 154–165.

564 <https://doi.org/10.1016/j.geoderma.2013.05.017>

565 Hvorslev, M. J. (1949). Subsurface exploration and sampling of soils for civil engineering
566 purposes. Waterways Experiment Station, Vicksburg

567 Kaestner, A., Schneebeli, M., & Graf, F. (2006). Visualizing three-dimensional root networks
568 using computed tomography. *Geoderma*, 136(1–2), 459–469.
569 <https://doi.org/10.1016/j.geoderma.2006.04.009>

570 Keller, T., Lamandé, M., Peth, S., Berli, M., Delenne, J. Y., Baumgarten, W., Rabbel, W., Radjaï,
571 F., Rajchenbach, J., Selvadurai, A. P. S., & Or, D. (2013). An interdisciplinary approach
572 towards improved understanding of soil deformation during compaction. *Soil and Tillage*
573 *Research*, 128, 61–80. <https://doi.org/10.1016/j.still.2012.10.004>

574 Ketcham, R. A., & Carlson, W. D. (2001). Acquisition, optimization and interpretation of x-ray
575 computed tomographic imagery: Applications to the geosciences. *Computers and*
576 *Geosciences*, 27(4), 381–400. [https://doi.org/10.1016/S0098-3004\(00\)00116-3](https://doi.org/10.1016/S0098-3004(00)00116-3)

577 Kroon, D.-J. (2010). *Hessian based Frangi Vesselness filter*
578 ([https://www.mathworks.com/matlabcentral/fileexchange/24409-hessian-based-frangi-](https://www.mathworks.com/matlabcentral/fileexchange/24409-hessian-based-frangi-vesselness-filter)
579 [vesselness-filter](https://www.mathworks.com/matlabcentral/fileexchange/24409-hessian-based-frangi-vesselness-filter)), *MATLAB Central File Exchange*.

580 Limaye, A. (2012). *Drishti: a volume exploration and presentation tool*. 85060X.
581 <https://doi.org/10.1117/12.935640>

582 Lin, H. (2010). Earth's Critical Zone and hydrogeology: Concepts, characteristics, and advances.
583 *Hydrology and Earth System Sciences*, 14(1), 25–45. <https://doi.org/10.5194/hess-14-25->

584
585
586
587
588
589
590
591
592
593
594
595
596
597
598
599
600
601
602
603

2010

Lucas, M., Schlüter, S., Vogel, H. J., & Vetterlein, D. (2019). Roots compact the surrounding soil depending on the structures they encounter. *Scientific Reports*, 9(1), 1–13. <https://doi.org/10.1038/s41598-019-52665-w>

Mairhofer, S., Zappala, S., Tracy, S. R., Sturrock, C., Bennett, M., Mooney, S. J., & Pridmore, T. (2012). RooTrak : Automated Recovery of Three-Dimensional Plant Root Architecture in Soil from X-Ray Microcomputed Tomography Images Using Visual Tracking. *Plant Physiology*, 158(February), 561–569. <https://doi.org/10.1104/pp.111.186221>

Menon, M., Mawodza, T., Rabbani, A., Blaud, A., Lair, G. J., Babaei, M., Kercheva, M., Rousseva, S., & Banwart, S. (2020). Pore system characteristics of soil aggregates and their relevance to aggregate stability. *Geoderma*, 366(February), 114259. <https://doi.org/10.1016/j.geoderma.2020.114259>

Menzies, J., van der Meer, J. J. M., & Ravier, E. (2016). A kinematic unifying theory of microstructures in subglacial tills. *Sedimentary Geology*, 344(April), 57–70. <https://doi.org/10.1016/j.sedgeo.2016.03.024>

Mitsch, W. J., & Gosselink, J. G. (1986). *Wetlands* (p. 539). Van Nostrand Reinhold, NY.

Moffett, K. B., Gorelick, S. M., McLaren, R. G., & Sudicky, E. A. (2012). Salt marsh ecohydrological zonation due to heterogeneous vegetation-groundwater-surface water interactions. *Water Resources Research*, 48(2). <https://doi.org/10.1029/2011WR010874>

Mooney, S. J. (2002). Three-dimensional visualization and quantification of soil macroporosity

604 and water flow patterns using computed tomography. *Soil Use and Management*, 18(2), 142–
605 151. <https://doi.org/10.1079/SUM2002121>

606 Naveed, M., Herath, L., Moldrup, P., Arthur, E., Nicolaisen, M., Norgaard, T., Ferré, T. P. A., &
607 de Jonge, L. W. (2016). Spatial variability of microbial richness and diversity and
608 relationships with soil organic carbon, texture and structure across an agricultural field.
609 *Applied Soil Ecology*, 103, 44–55. <https://doi.org/10.1016/j.apsoil.2016.03.004>

610 Ngom, N. F., Garnier, P., Monga, O., & Peth, S. (2011). Extraction of three-dimensional soil pore
611 space from microtomography images using a geometrical approach. *Geoderma*, 163(1–2),
612 127–134. <https://doi.org/10.1016/j.geoderma.2011.04.013>

613 Pedersen, L. L., Smets, B. F., & Dechesne, A. (2015). Measuring biogeochemical heterogeneity at
614 the micro scale in soils and sediments. *Soil Biology and Biochemistry*, 90, 122–138.
615 <https://doi.org/10.1016/j.soilbio.2015.08.003>

616 Persson, H. A. (2012). The High Input of Soil Organic Matter from Dead Tree Fine Roots into the
617 Forest Soil. *International Journal Of Forestry Research*, 2012.
618 <https://doi.org/10.1155/2012/217402>

619 Pezeshki, S. R., & DeLaune, R. D. (2012). Soil Oxidation-Reduction in Wetlands and Its Impact
620 on Plant Functioning. *Biology*, 1(3), 196–221. <https://doi.org/10.3390/biology1020196>

621 Phillips, E. R., Evans, D. J. A. E., van der Meer, J. J. M., & Lee, J. R. (2018). Microscale evidence
622 of liquefaction and its potential triggers during soft-bed deformation within subglacial
623 traction tills. *Quaternary Science Review*, 181, 123–143.

624 Pöhlitz, J., Rücknagel, J., Koblenz, B., Schlüter, S., Vogel, H. J., & Christen, O. (2018). Computed
625 tomography and soil physical measurements of compaction behaviour under strip tillage,
626 mulch tillage and no tillage. *Soil and Tillage Research*, 175(September 2017), 205–216.
627 <https://doi.org/10.1016/j.still.2017.09.007>

628 Pot, V., Zhong, X., & Baveye, P. C. (2020). Effect of resolution, reconstruction settings, and
629 segmentation methods on the numerical calculation of saturated soil hydraulic conductivity
630 from 3D computed tomography images. *Geoderma*, 362(May 2019), 114089.
631 <https://doi.org/10.1016/j.geoderma.2019.114089>

632 Rabot, E., Wiesmeier, M., Schlüter, S., & Vogel, H. J. (2018). Soil structure as an indicator of soil
633 functions: A review. *Geoderma*, 314(October 2017), 122–137.
634 <https://doi.org/10.1016/j.geoderma.2017.11.009>

635 Ray, A. (2011). CT pro user manual. *Nikon Metrology, Hertfordshire, England*.

636 Rogers, E. D., & Benfey, P. N. (2015). Regulation of plant root system architecture: Implications
637 for crop advancement. *Current Opinion in Biotechnology*, 32(Figure 1), 93–98.
638 <https://doi.org/10.1016/j.copbio.2014.11.015>

639 Rogers, E. D., Monaenkova, D., Mijar, M., Nori, A., Goldman, D. I., & Benfey, P. N. (2016). X-
640 ray computed tomography reveals the response of root system architecture to soil texture.
641 *Plant Physiology*, 171(3), 2028–2040. <https://doi.org/10.1104/pp.16.00397>

642 Schindelin, J., Arganda-Carreras, I., Frise, E., Kaynig, V., Longair, M., Pietzsch, T., Preibisch, S.,
643 Rueden, C., Saalfeld, S., Schmid, B., Tinevez, J. Y., White, D. J., Hartenstein, V., Eliceiri,
644 K., Tomancak, P., & Cardona, A. (2012). Fiji: An open-source platform for biological-image

645 analysis. *Nature Methods*, 9(7), 676–682. <https://doi.org/10.1038/nmeth.2019>

646 Schlüter, S., Weller, U., & Vogel, H. J. (2010). Segmentation of X-ray microtomography images
647 of soil using gradient masks. *Computers and Geosciences*, 36(10), 1246–1251.
648 <https://doi.org/10.1016/j.cageo.2010.02.007>

649 Schulz, H., Postma, J. A., van Dusschoten, D., Scharr, H., & Behnke, S. (2013). Plant Root System
650 Analysis from MRI Images. *Communications in Computer and Information Science*, 359
651 *CCIS*, 411–425. https://doi.org/10.1007/978-3-642-38241-3_28

652 Smith, K. A., Ball, T., Conen, F., Dobbie, K. E., Massheder, J., & Rey, A. (2003). Exchange of
653 greenhouse gases between soil and atmosphere. *European Journal of Soil Science*,
654 54(December), 779–791. <https://doi.org/10.1046/j.1365-2389.2003.00567.x>

655 Spagnolo, M., Phillips, E., Piotrowski, J. A., Rea, B. R., Clark, C. D., Stokes, C. R., Carr, S. J.,
656 Ely, J. C., Ribolini, A., Wysota, W., & Szuman, I. (2016). Ice stream motion facilitated by a
657 shallow-deforming and accreting bed. *Nature Communications*, 7.
658 <https://doi.org/10.1038/ncomms10723>

659 Spencer, K. L., Carr, S. J., Diggins, L. M., Tempest, J. A., Morris, M. A., & Harvey, G. L. (2017).
660 The impact of pre-restoration land-use and disturbance on sediment structure, hydrology and
661 the sediment geochemical environment in restored saltmarshes. *Science of the Total*
662 *Environment*, 587–588, 47–58. <https://doi.org/10.1016/j.scitotenv.2016.11.032>

663 Swanson, S., Kozłowski, D., Hall, R., Heggem, D., & Lin, J. (2017). Riparian proper functioning
664 condition assessment to improve watershed management for water quality. *Journal of Soil*
665 *and Water Conservation*, 72(2), 168–182. <https://doi.org/10.1016/j.hal.2017.06.001>.Submit

666 Taina, I. A., Heck, R. J., & Elliot, T. R. (2008). Application of X-ray computed tomography to soil
667 science: A literature review. *Canadian Journal of Soil Science*, 88(1), 1–19.
668 <https://doi.org/10.4141/CJSS06027>

669 Tarplee, M. F. V., van der Meer, J. J. M., & Davis, G. R. (2011). The 3D microscopic “signature”
670 of strain within glacial sediments revealed using X-ray computed microtomography.
671 *Quaternary Science Reviews*, 30(23–24), 3501–3532.
672 <https://doi.org/10.1016/j.quascirev.2011.05.016>

673 Teixeira, A., Duarte, B., & Caçador, I. (2014). Salt Marshes and Biodiversity. In *Sabkha*
674 *Ecosystems: Volume IV: Cash Crop Halophyte and Biodiversity Conservation* (Vol. 47, pp.
675 283–298). <https://doi.org/10.1007/978-94-007-7411-7>

676 Turner, R. E. (2004). Coastal wetland subsidence arising from local hydrologic manipulations.
677 *Estuaries*, 27(2), 265–272. <https://doi.org/10.1007/BF02803383>

678 van Marcke, P., Verleye, B., Carmeliet, J., Roose, D., & Swennen, R. (2010). An Improved Pore
679 Network Model for the Computation of the Saturated Permeability of Porous Rock. *Transport*
680 *in Porous Media*, 85(2), 451–476. <https://doi.org/10.1007/s11242-010-9572-1>

681 Voepel, H., Leyland, J., Hodge, R. A., Ahmed, S., & Sear, D. (2019). Development of a vector-
682 based 3D grain entrainment model with application to X-ray computed tomography scanned
683 riverbed sediment. *Earth Surface Processes and Landforms*, 44(15), 3057–3077.
684 <https://doi.org/10.1002/esp.4608>

685 Wildenschild, D., & Sheppard, A. P. (2013). X-ray imaging and analysis techniques for
686 quantifying pore-scale structure and processes in subsurface porous medium systems.

687 *Advances in Water Resources*, 51, 217–246. <https://doi.org/10.1016/j.advwatres.2012.07.018>

688 Xiong, Y., Ola, A., Phan, S. M., Wu, J., & Lovelock, C. E. (2019). Soil Structure and Its
689 Relationship to Shallow Soil Subsidence in Coastal Wetlands. *Estuaries and Coasts*, 42(8),
690 2114–2123. <https://doi.org/10.1007/s12237-019-00659-2>

691 Young, D. (2014). *Canny edge detection in 2-D and 3-D*
692 ([https://www.mathworks.com/matlabcentral/fileexchange/45459-canny-edge-detection-in-2-](https://www.mathworks.com/matlabcentral/fileexchange/45459-canny-edge-detection-in-2-d-and-3-d)
693 [d-and-3-d](https://www.mathworks.com/matlabcentral/fileexchange/45459-canny-edge-detection-in-2-d-and-3-d)), *MATLAB Central File Exchange*.

694 Zappala, S., Mairhofer, S., Tracy, S., Sturrock, C. J., Bennett, M., Pridmore, T., & Mooney, S. J.
695 (2013). Quantifying the effect of soil moisture content on segmenting root system architecture
696 in X-ray computed tomography images. *Plant and Soil*, 370(1–2), 35–45.
697 <https://doi.org/10.1007/s11104-013-1596-1>

698